INORGANIC CHEMISTRY FRONTIERS

RESEARCH ARTICLE

View Article Online
View Journal | View Issue

Cite this: *Inorg. Chem. Front.*, 2024, **11**, 8123

Multicolor luminescence and afterglow from $Cs_2NaScCl_6:Sb^{3+},Mn^{2+}$ crystals†

Xiaojia Wang, [a] Wei Zheng,[b] Xiangzhou Zhang,[a] Xiangxiang Chen[a] and Yuhai Zhang *[a]

In contrast to single-band emitting phosphors, dual-band emitting phosphors provide a versatile tool for ratio-metric color tuning, enabling a wide color gamut and ensuing applications in information encryption and the anti-counterfeiting area. Here, a double perovskite, $Cs_2NaScCl_6:xMn^{2+}$ single crystals, was grown by a hydrothermal method. Pristine $Cs_2NaScCl_6$ crystals exhibited a pure blue emission band originating from the self-trapped excitons. Upon doping with Mn^{2+}, the crystals exhibited a dual-band emission profile, consisting of both STE and Mn^{2+} emissions. To this end, the ratio of two bands was manipulated with Mn^{2+}-doping concentration, rendering a wide color gamut from blue to red. Interestingly, co-doping with Sb^{3+} ions significantly enhanced the overall photoluminescence, boosting the quantum yield from 8.8% to up to 62.4%. Such an enhancement is attributed to an efficient energy transfer process from the STE to Mn^{2+} based on an investigation of photoluminescence lifetime. Importantly, these crystals exhibited an intriguing afterglow after X-ray excitation, with a duration exceeding 3000 s. This remarkable phenomenon opens up many new possibilities for their application in the advanced anti-counterfeiting area.

Received 8th August 2024,
Accepted 30th September 2024

DOI: 10.1039/d4qi02019g

rsc.li/frontiers-inorganic

1. Introduction

Chloride-based perovskite crystals are a typical wide-bandgap semiconductor material with a high tolerance towards heterovalence doping with various impurity ions, including cationic activators (Cu^+, Mn^{2+}, rare earth ions) and anionic substitution (Cl^-, Br^-, I^-).[1–6] The doping not only introduces new luminescence centers but also creates abundant defect states.[7–12] Mn^{2+} ions exhibit visible light emission due to the $^4T_1 \rightarrow {}^6A_1$ transition, which is highly sensitive to the crystal field environment. To this end, Mn^{2+} has a spectral tuning ability from green to red by adjusting the coordination number from 4 to 6.[13,14] In addition, the lifetime of Mn^{2+} emission is substantially long, extending to several milliseconds, which provides an ideal platform for time-gated imaging which is free of background noise.[15]

Apart from the multicolor emission, the Mn^{2+} ions feature a multi-band excitation profile.[16] The PL excitation spectra ranges from 300 nm to 550 nm, corresponding to a series of characteristic $^6A_1(^6S)$ transitions to $^4T_1(^4P)$, $^4E_g(^4D)$, $^4T_{2g}(^4D)$, $^4A_1(^4G)$, $^4E(^4G)$, $^4T_{2g}(^4G)$, and $^4T_{1g}(^4G)$ states. Such a discrete pattern allows a high freedom of excitation choice, providing added protection for anti-counterfeiting applications.[17,18] Besides, the excitation has been extended to the X-ray band recently. Xia *et al.* reported a phosphor of $CsCdCl_3:Mn^{2+},R^{4+}$ (R = Ti, Zr, Hf and Sn) for X-ray storage, demonstrating an afterglow of 12 hours and a spatial resolution of 12.5 mm lp^{-1} for X-ray imaging. Importantly, such a phosphor featuring a time-lapse manner is convenient for three-dimensional X-ray imaging of a curved body.[19] Han *et al.* reported an X-ray excitable persistent luminescence by introducing Li^+ into the $Zn_2GeO_4:Mn^{2+}$ phosphor. Compared to single-mode encryption, orthogonal encryptions significantly enhanced the security of anti-counterfeiting as benefited from the independent readout in each mode.[20] Our group recently synthesized transparent perovskite crystals of $Cs_2NaInCl_6:Mn^{2+}$, showing the potential of X-ray excitable afterglow for advanced three-dimensional information encryption.[21] One drawback of the Mn^{2+}-activated phosphor is the single emission band, which limits its anti-counterfeiting application in multicolor encryption.

In this work, a hydrothermal method was used to synthesize $Cs_2NaScCl_6:xMn^{2+}$ single crystals. A pure blue emission band of self-trapped excitons (STEs) was observed from pristine $Cs_2NaScCl_6$ crystals. After Mn^{2+} doping, the crystals exhibited a dual-band emission of both STE and Mn^{2+} emissions, which rendered a multicolor luminescence by adjusting

[a]*Institute for Advanced Interdisciplinary Research (iAIR), School of Chemistry and Chemical Engineering, University of Jinan, Jinan 250022, Shandong, P. R. China. E-mail: ifc_zhangyh@ujn.edu.cn*
[b]*School of Materials Science and Engineering, Shandong University, Jinan 250061, Shandong, P. R. China*

† Electronic supplementary information (ESI) available. See DOI: https://doi.org/10.1039/d4qi02019g

their ratio. Interestingly, the introduction of Sb^{3+} ions significantly enhanced the dual-band emissions, leading to a boost in the photoluminescence quantum yield (PL QY) from 8.8% to 62.4%, where the energy transfer (ET) process from the self-trapping exciton to Mn^{2+} played a critical role. Importantly, the crystals showed an afterglow after X-ray excitation, which lasted for more than 3000 s.

2. Results and discussion

$Cs_2NaScCl_6$:1%Sb^{3+},x%Mn^{2+} single crystals were grown in a hydrothermal reactor where a programmable cooling procedure (~3 °C h^{-1}) was applied to regulate the crystallization. The size of the as-prepared crystals was in the range from 1 to 5 mm, which was closely related to the cooling rate.[22,23] As shown in Fig. 1a, the powder X-ray diffraction (XRD) patterns were well indexed to the standard diffraction pattern of $Cs_2NaScCl_6$ (CCDC 2054287). It should be noted that 1%-Sb^{3+} doping did not introduce any remarkable shift in the XRD peaks. Further doping with Mn^{2+} beyond the 30 mol% nominal feeding concentration in the precursor, however, generated an impurity phase of NaCl. Next, inductively coupled plasma (ICP) measurements were performed to identify the actual dopant concentration in the crystals (Table S1†). The actual concentration of Mn was 2.11 mol%, which was much lower than the nominal feeding concentration (20 mol%), largely due to the hetero-valence doping effect between Mn^{2+} and Sc^{3+}.[21] Compared with the Na^+ ion (1.02 Å) and Cs^+ ion (1.67 Å), the doped Mn^{2+} ion (0.83 Å) has a ionic radius closer to the Sc^{3+} ion (0.75 Å). In this sense, Mn^{2+} prefers to substitute the Sc^{3+} site in the lattice.

Despite the trace-amount of Mn^{2+} or Sb^{3+}, the optical properties of $Cs_2NaScCl_6$:1%Sb^{3+},x%Mn^{2+} crystals were significantly modified. In particular, the doping of Sb^{3+} or Mn^{2+} separately into the $Cs_2NaScCl_6$ matrix significantly enhanced its photoluminescence. The ensuing PL QY increased from 3.2% to 23.8% after 1 mol% Sb^{3+} doping due to the distortion of the octahedron (Fig. 1b and Fig. S1†).[24,25] In comparison, the introduction of Mn^{2+} yielded not only a distinct red emission but also an enhanced PL QY from 3.2% to 8.8% (Fig. S2†). Interestingly, when Mn^{2+} and Sb^{3+} were co-doped, the PL QY showed a significant increase of up to 62.4%. Due to the emergence of the red

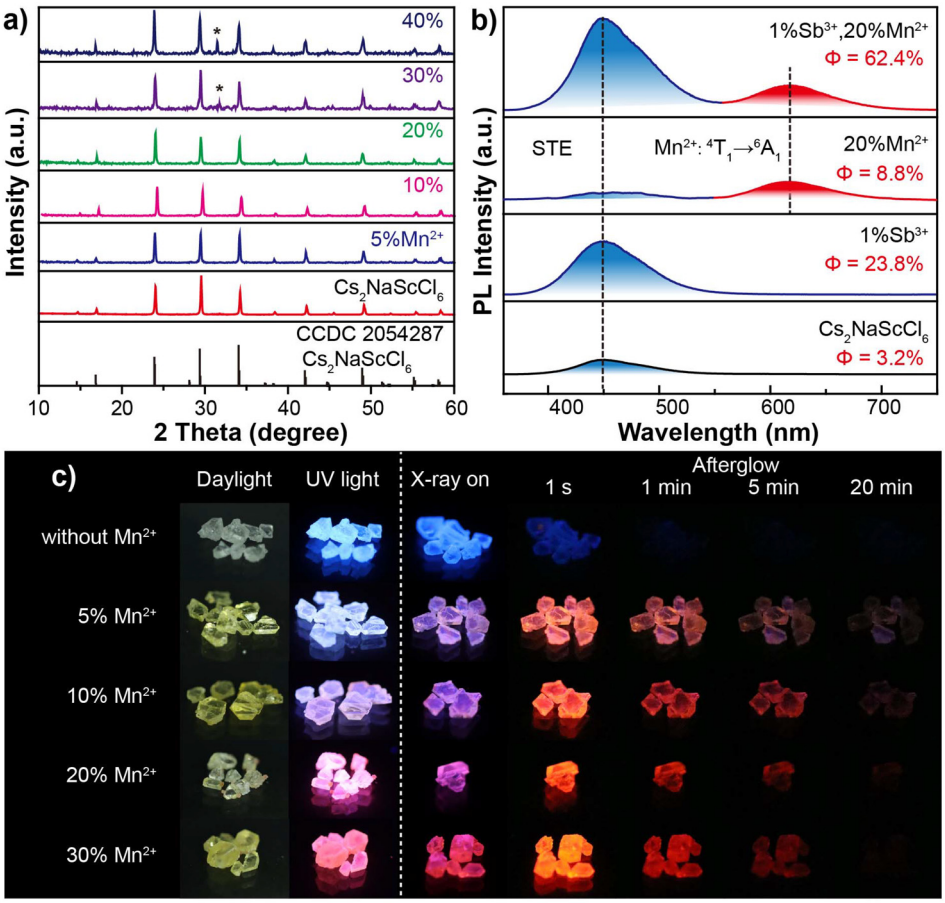

Fig. 1 Structure and luminescence of $Cs_2NaScCl_6$:1%Sb^{3+},x%Mn^{2+} crystals. (a) X-ray diffraction patterns showed a high phase purity below 20% Mn^{2+}-doping. The asterisk (*) marks an impurity phase of NaCl. (b) Steady-state PL spectra show a boosted PL QY of up to 62.4% after co-doping with both Mn^{2+} and Sb^{3+}. (c) Photographs of the crystals under daylight, 365 nm UV light and X-ray, respectively. The X-ray-induced afterglow are shown in photographs on the right panel.

peak, the crystals exhibited a wide color gamut upon Mn-doping (Fig. 1c). Besides ultraviolet light, X-ray was found to be another effective excitation source. It should be noted that the red component in the radioluminescence (RL) profile was higher than that in PL spectra (Fig. S3†).

Apart from RL, the doped crystals exhibited an intense afterglow after ceasing the X-ray excitation. The crystals without Mn^{2+} doping exhibited a strong blue emission under X-ray excitation. Once the X-ray source was turned off, the blue RL decayed rapidly, indicating a weak afterglow. In stark contrast, the Mn-doped crystals exhibited a strong red afterglow, suggesting the key role of Mn^{2+} ions in activating the afterglow traps in halide crystals.[26] Remarkably, the afterglow signal in darkness could be clearly captured using a commercial camera (Canon 90D) even after a 20 min delay (Fig. 1c).

To shed light on the energy transfer (ET) process between dopants, steady-state PL spectra of varied crystals were collected under 340 nm excitation. The PL spectra showed a dual-band profile, suggesting the presence of two luminescence centers. The blue emission (~450 nm) was attributed to the STE emission of the host, while the red emission (~620 nm) was attributed to the $^4T_1 \rightarrow {}^6A_1$ transition of Mn^{2+} (Fig. 2a and Fig. S4†). With the constant Sb^{3+}-doping concentration, the red band increased with an increasing Mn^{2+}-content, indicating the possibility of stable energy transfer from the STE state to Mn^{2+} (Fig. 2b). In fact, the red component increased up to 55.4% of the total emission intensity in the heavy Mn^{2+}-doping region (~60 mol%). Concurrently, the PL QY was elevated to a maximum of 62.4% at 20 mol% of Mn^{2+} doping. To this end, the nonradiative recombination by the quenchers (Q1) was outperformed by the energy cascade from free exciton (FE) to the STE, and then to Mn^{2+}. However, when the Mn^{2+} doping concentration exceeded 30 mol%, non-emitting red crystals (as shown by dashed circles in Fig. S5†) were observed, suggesting an uneven Mn-element distribution in the product. Due to the concentration quenching effect, a further increase of Mn^{2+} would lead to a decrease in the PL QY (Fig. 2b).

To further confirm the ET process, the excitation–emission map was collected for Sb^{3+} and Mn^{2+} co-doped crystals (Fig. 2c). The map clearly showed two excitation centers at ~280 nm and ~340 nm, belonging to the characteristic transitions from $^1S_0$ to $^3P_2$ and $^3P_1$ of Sb^{3+}, respectively (Fig. S6†). Such transition was effective in exciting the blue band since Sb^{3+} intrinsically localized the STE, which echoed well with previous reports.[27,28] It is worth noting that although the weak blue emission from the host STE showed a complete overlap with Sb^{3+} activated emission, they are not from the same origin since their excitation spectra largely differed as shown in Fig. S6c.† Intriguingly, such an excitation was found to be equally effective to stimulate the red band from Mn^{2+}, providing strong evidence for the energy

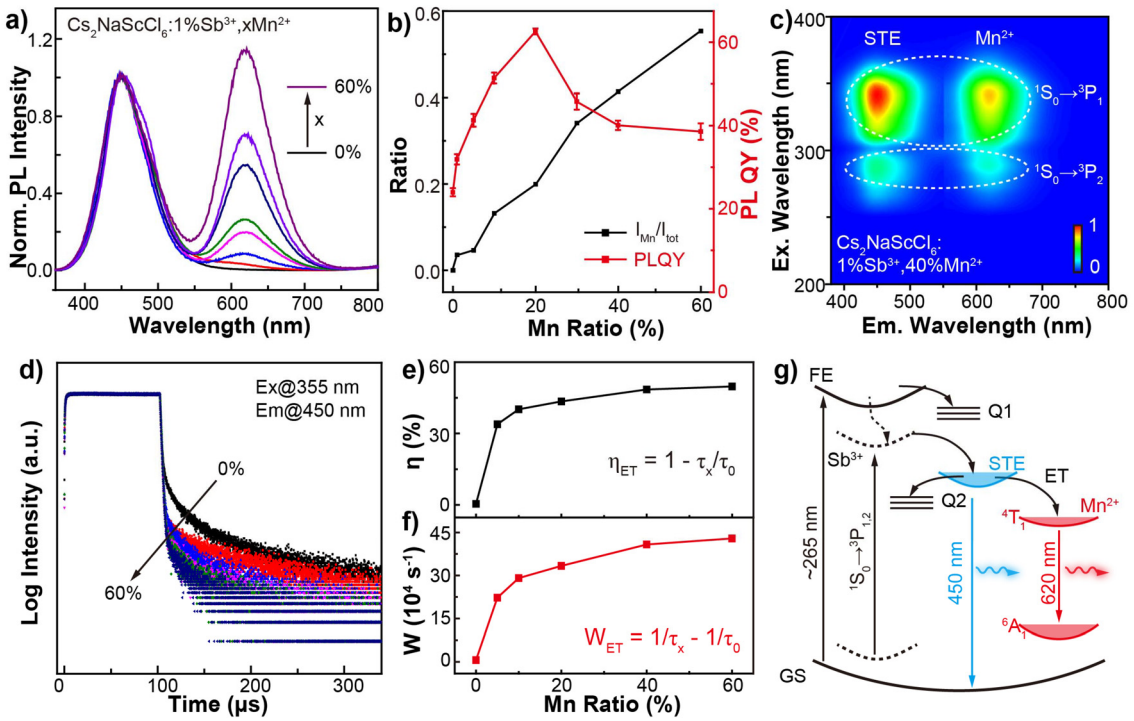

Fig. 2 Investigation of the ET process in $Cs_2NaScCl_6$:1%Sb^{3+},xMn^{2+} crystals. (a) Steady-state PL spectra under 340 nm excitation of crystals with varied Mn^{2+}-doping concentrations. The spectra were normalized at 450 nm, which showed a decrease in the PL ratio of the STE and an increase in the PL ratio of Mn^{2+} (b, black dot plot). (b, red dot plot) PL QYs for a series of the $Sb^{3+}$and Mn^{2+} doped crystals. (c) Excitation–emission mapping of $Cs_2NaScCl_6$:1%Sb^{3+},40%Mn^{2+} crystals. (d) Photoluminescence decay curves for the STE emission (450 nm). (e and f) Dependence of the energy transfer rate (W_{ET}) and efficiency (η_{ET}) on the Mn^{2+}-doping concentration. (g) Energy level diagram of $Cs_2NaScCl_6$:1%Sb^{3+},xMn^{2+} crystals and the proposed luminescence mechanism.

transfer from the STE to Mn^{2+}. To further verify the ET process, the lifetime of STE emission was monitored with increasing Mn^{2+}-content (Fig. 2d and Fig. S7†). With the increase in Mn^{2+}-doping concentration, the lifetime (τ_x, x is the Mn^{2+}-doping concentration) decreased from 2.35 μs to 1.17 μs (Table S2†). Accordingly, the energy transfer rate (W_{ET}) changed from 22.0 × 10^4 s^{-1} to 42.9 × 10^4 s^{-1}, and the energy transfer efficiency (η_{ET}) reached 50.2% (Fig. 2e and f). Based on the above result, a possible luminescence mechanism of Sb^{3+} and Mn^{2+} co-doped crystals is proposed in Fig. 2g. New electronic transition channels ($^3P_2$ and $^3P_1$ of Sb^{3+}) were introduced at 280 and 340 nm due to the doping of Sb^{3+} ions. These channels competed with the quenchers (Q1), whereby the energy of free excitons was effectively transferred to the STE emitters. In addition, there was an efficient ET process from STE to Mn^{2+} emitters, which outperformed the quenchers (Q2). This route not only enhanced the Mn^{2+} emission but also increased the overall PL QY.

To investigate the electron–phonon coupling effect, temperature-dependent PL spectra were recorded for a co-doped crystal (Fig. 3a and Fig. S8c†). Its STE emission was significantly robust against thermal quenching, which is quite different from that of the Mn^{2+}-free crystal (Fig. S8a and b†). Instead, the Mn^{2+} emission was severely quenched at elevated temperatures, showing an identical thermal quenching profile to that of Sb^{3+}-activated crystals. Indeed, by fitting the temperature-dependent PL intensity, the exciton binding energy (E_a) of STE and Mn^{2+} could be calculated to be 45.5 meV and 44.0 meV, respectively (Fig. S9†).[29] The similar E_a evidenced the clear energy-cascade route from the STE to Mn^{2+}. To quantitatively understand the electron–phonon coupling strength, the full-width-at-half-maxima (FWHM) of emission peaks were fitted against the temperature (Fig. 3b). When the temperature increased from 93 K to 473 K, the FWHM of the STE emission increased from 360 meV to 510 meV, showing an evident thermal broadening. The Huang–Rhys factor, S, was obtained by fitting the following eqn (1):[30]

$$\mathrm{FWHM} = 2.36\sqrt{S}\hbar\omega\sqrt{\coth\left(\frac{\hbar\omega}{2kT}\right)} \quad (1)$$

where $\hbar\omega$ is the phonon energy, k is the Boltzmann constant, and T is the temperature. The value of S for STE emission was about 12.8, suggesting that 12.8 phonons (43.4 meV, 350 cm^{-1}) were generated in every single radiative transition of STE emission.[31,32] To shed more light on the preferred vibrational modes, Raman spectra of the single crystal were collected under 532 nm laser excitation (Fig. 3c). Three characteristic peaks at 197 (T_{2g}), 260 (E_g), and 343 cm^{-1} (A_{1g}) were ascribed to the breathing, asymmetric stretching, and symmetric stretching modes of the vibrational $[ScCl_6]^{3-}$ octahedron, respectively.[33,34] Therefore, the STE transition was found to be preferable to couple with the symmetric stretching of octahedra. Concurrently, the Mn^{2+} emission was found to be favorable to couple with the asymmetric stretching vibrations (32.2 meV, 260 cm^{-1}). However, the coupling strength (S = 7.2) was weaker than that of the STE emission due to the partially shielded d–d transition.[35] Interestingly, the STE band showed a red shift upon heating, which was opposite to the Mn^{2+} band (Fig. S8d†). The red shift was attributed to the thermal expansion of the lattice. In contrast, the blue shift of the Mn^{2+} emission was caused by the participation of phonons. With the aid of phonons, electrons were promoted to a higher energy level with the increasing temperature, resulting in a blue shift in the emission band.

Apart from the photoluminescence, the crystals exhibited a strong radioluminescence under X-ray excitation. The RL spectra showed a similar profile to the PL spectra, including both STE and Mn^{2+} emissions. However, their intensity ratio varied significantly with the Mn^{2+}-content, which suggested a wider color gamut under X-ray excitation (Fig. 4a and Fig. S10†). Intriguingly, $Cs_2NaScCl_6$:1%Sb^{3+},$x$$Mn^{2+}$ crystals continued to glow after the radiation ceased. In fact, the afterglow remained two orders of magnitude higher than the background noise after a 3000 s delay (Fig. 4b) for all samples with varied Mn^{2+} contents. The afterglow profile was identical to the RL spectra, consisting of both STE and Mn^{2+} bands. While the Mn^{2+} band was usually attributed to the $^4T_1 \rightarrow {}^6A_1$ transition, the STE band was quite novel.[36]

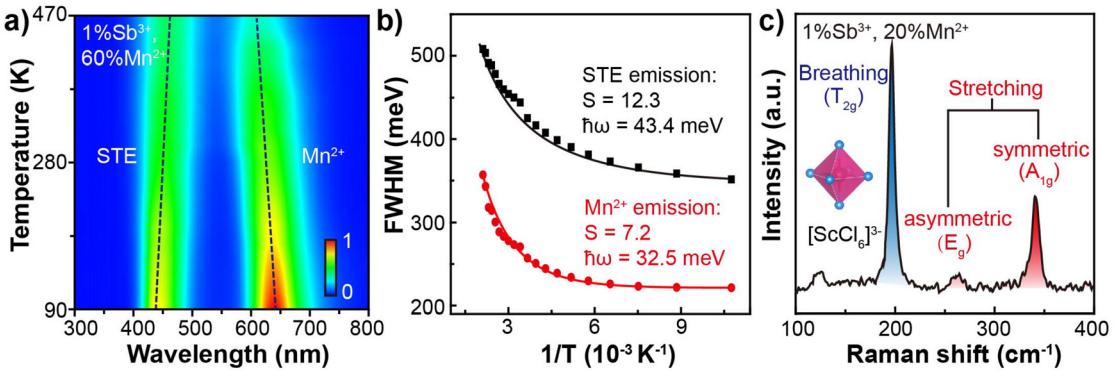

Fig. 3 Temperature-dependent emission of $Cs_2NaScCl_6$:1%Sb^{3+},60%Mn^{2+} crystals. (a) Pseudo color mapping of temperature-dependent PL spectra under 365 nm excitation of Mn-doped crystals. (b) The FWHM of the STE and Mn^{2+} emission is plotted as a function of temperature. (c) Raman spectrum of the $Cs_2NaScCl_6$:1%Sb^{3+},60%Mn^{2+} crystals.

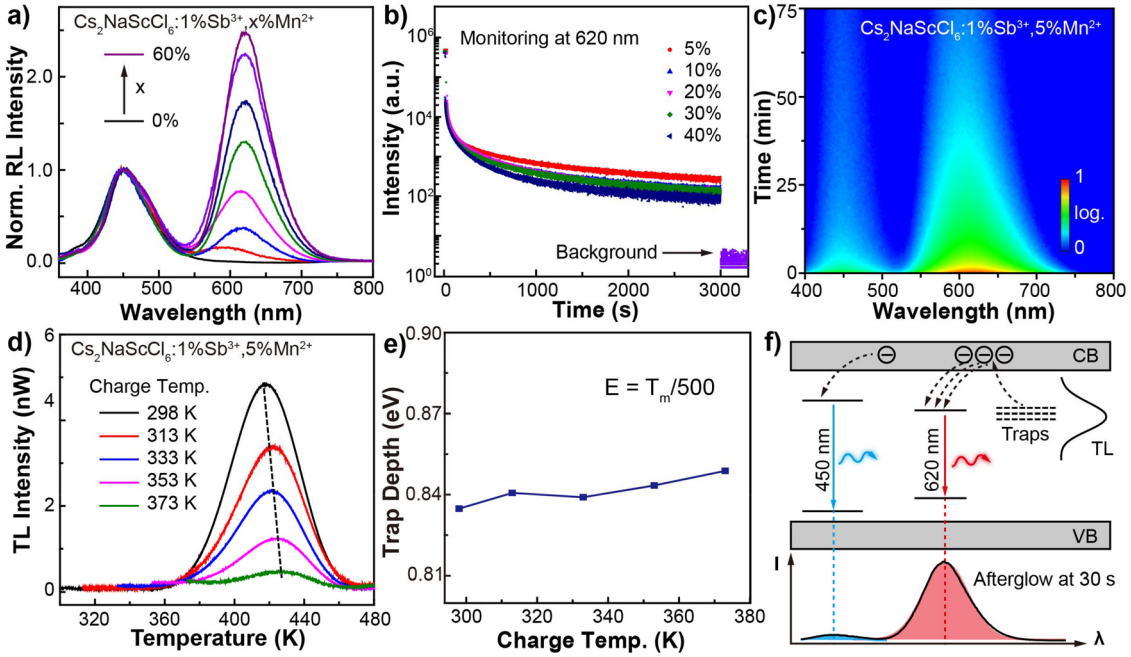

Fig. 4 Radioluminescence (RL) afterglow of $Cs_2NaScCl_6$:1%Sb^{3+},x%Mn^{2+} crystals. (a) X-ray excited radioluminescence spectra of crystals with varied Mn^{2+}-doping concentrations. (b) Afterglow decay curves of crystals with varied Mn^{2+}-doping concentrations. (c) Time-resolved afterglow spectra were similar to the RL spectrum, but the STE emission decayed faster than the Mn^{2+} emission. (d) TL curves were collected at different charging temperatures (298–373 K) at a heating rate of 2.5 K s^{-1}. The trap depth of TL centers was calculated and displayed in (e). (f) Schematic diagram of the luminescence mechanism of $Cs_2NaScCl_6$:1%Sb^{3+},5%Mn^{2+} crystals.

In order to understand the afterglow properties, the distribution of active traps was probed through a thermoluminescence experiment. It should be noted that the active traps refer to those where carriers can escape under thermal vibration and recombine to produce afterglow photons. The thermoluminescence curves were recorded *via* a thermal cleaning method (Fig. 4d). Typically, the TL curves were obtained with a heating rate of 2.5 K s^{-1} after X-ray charging for 1 min at different temperatures (298–373 K). The empirical formula $E = T_m/500$ was used to estimate the trap depth. The trap depth remained essentially identical with the increase of charging temperature, indicating only one active trap in the TL process (Fig. 4e).[37] Concurrently, the shape of TL curve remained identical while the intensity saturated after 5 min of charging (Fig. S11†). Based on the above discussion, we proposed a possible afterglow mechanism as shown in Fig. 4f. The incor-

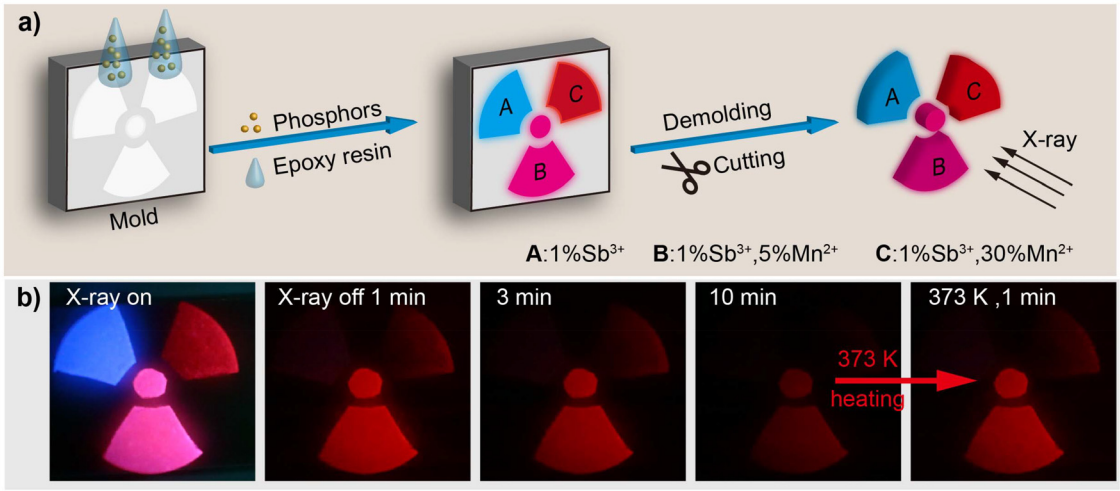

Fig. 5 The anti-counterfeiting pattern of multicolor $Cs_2NaScCl_6$:1%Sb^{3+},x%Mn^{2+} phosphors. (a) Fabrication processes of the anti-counterfeiting pattern. (b) Radioluminescence photographs of the pattern, showing a dynamic luminescence as time evolves.

poration of Mn^{2+} as impurity ions into the crystals significantly increased the number of active traps, whereby more excited electrons were trapped upon excitation. The electrons were stimulated by phonons and de-trapped to the conduction band as FEs. Thereafter, the energy of FE transferred to both STE and Mn^{2+}, where the radiative transition generated the afterglow emission.

The multicolor feature of the crystals provided a facile tool for advanced anti-counterfeiting applications. To this end, we prepared three crystals using varied doping strategies, exhibiting blue, red, and pink under X-ray excitation. The crystals were first ground into powders and then mixed with epoxy resin. After filling, drying, demolding and cutting, anti-counterfeiting patterns with different Mn^{2+} contents were obtained (Fig. 5a). Due to the different Mn^{2+} contents, they not only showed a multicolor tint under excitation but also exhibited an extended afterglow after ceasing the excitation. Importantly, the red afterglow could recover through thermal stimulation, which provided added protection to the encrypted information (Fig. 5b).

3. Conclusion

In this work, $Cs_2NaScCl_6$:1%Sb^{3+},xMn^{2+} crystals were synthesized by a hydrothermal method. Multicolor luminescence and ensuing afterglow were activated by doping with Mn^{2+} ions. Importantly, further doping with Sb^{3+} ions significantly boosted the PL QY up to 62.4% through quencher passivation, as evidenced from time-resolved spectroscopy. The multicolor luminescence and dynamic afterglow enabled a sophisticated encoding technique, opening many possibilities to advanced applications including information encryption and anti-counterfeiting.

Data availability

Data for this article, including Fig. 1a, b, Fig. 2a–e, Fig. 3a, b, and Fig. 4a–e† are available at Science Data Bank at **https://doi.org/10.57760/sciencedb.11546**.

Conflicts of interest

All authors declare that they have no competing interests.

Acknowledgements

This work is financially supported by the Natural Science Foundation of Shandong Province (No. ZR2023JQ026) and the 20-Iterm Project in Universities of Jinan city (No. 202228091).

References

1 X.-G. Zhao, D. Yang, J.-C. Ren, Y. Sun, Z. Xiao and L. Zhang, Rational Design of Halide Double Perovskites for Optoelectronic Applications, *Joule*, 2018, **2**, 1662–1673.
2 X. Wang, X. Zhang, S. Yan, H. Liu and Y. Zhang, Nearly-Unity Quantum Yield and 12-Hour Afterglow from a Transparent Perovskite of $Cs_2NaScCl_6$:Tb, *Angew. Chem., Int. Ed.*, 2022, **61**, e202210853.
3 N. Liu, W. Zheng, R. Sun, X. Li, X. Xie, L. Wang and Y. Zhang, Near–Infrared Afterglow and Related Photochromism from Solution–Grown Perovskite Crystal, *Adv. Funct. Mater.*, 2021, **32**, 2110663.
4 H. You, G. Guan, T. Lang, M. Cai, P. Su, H. He, Y. Zhong and T. Han, High Thermally Stable Deep Red-Emitting Sb^{3+},Ho^{3+}-Codoped $Cs_2NaScCl_6$ Double Perovskite for Plant Lighting, *J. Rare Earths*, 2023, DOI: **10.1016/j.jre.2023.10.012**.
5 K. Jiang, Y. Wang, C. Lin, L. Zheng, J. Du, Y. Zhuang, R. Xie, Z. Li and H. Lin, Enabling Robust and Hour-Level Organic Long Persistent Luminescence from Carbon Dots by Covalent Fixation, *Light: Sci. Appl.*, 2022, **11**, 80.
6 Y. Zhang, S. Yan, F. Xiao, X. Shan, X. Lv, W. Wang and Y. Liang, Long-Persistent Far-Uvc Light Emission in Pr^{3+}-Doped $Sr_2P_2O_7$ Phosphor for Microbial Sterilization, *Inorg. Chem. Front.*, 2023, **10**, 5958–5968.
7 Y. Chen, J. Wu, S. Zhang, X. Zhu, B. Zou and R. Zeng, Effective Energy Transfer Boosts Emission of Rare-Earth Double Perovskites: The Bridge Role of Sb(III) Doping, *J. Phys. Chem. Lett.*, 2023, **14**, 7108–7117.
8 D. Liang, H. Xiao, W. Cai, S. Lu, S. Zhao, Z. Zang and L. Xie, Mn^{2+}-Based Luminescent Metal Halides: Syntheses, Properties, and Applications, *Adv. Opt. Mater.*, 2023, **11**, 2202997.
9 Y. Shao, H. Cai, F. Zhao, Z. Song and Q. Liu, Efficient Blue–Violet Phosphor with Small Stokes-Shift for Full-Spectrum Lighting, *Laser Photonics Rev.*, 2023, **17**, 2300342.
10 A. Huang, M. Liu, C.-K. Duan, K.-L. Wong and P. A. Tanner, Understanding the Ultraviolet, Green, Red, near Infrared and Infrared Emission Properties of Bismuth Halide Double Perovskite, *Inorg. Chem. Front.*, 2022, **9**, 6379–6390.
11 X. Jiang, H. Ding, F. Yang, F. Luo, Z. Gan, Z. Fan, F. Gao, Z. Cheng, G. Luo and W. Zhou, Sb^{3+}/Sm^{3+} Codoped $Cs_2NaScCl_6$ All-Inorganic Double Perovskite: Blue Emission of Self-Trapped Excitons and Red-Emission Via Energy Transfer, *Inorg. Chem.*, 2024, **63**, 10756–10766.
12 W. Li, Y. Wang, H. Yin, J. Chen, K. Han, F. Liu and R. Zhang, Excitation-Dependent Emission in Sb^{3+}-Doped All-Inorganic Rare-Earth Double Perovskites for Anticounterfeiting Applications, *Inorg. Chem.*, 2024, **63**, 10481–10489.
13 Y.-H. Liu, X. Yan, L. Xiao, W. Jiang, Q. Liu, T.-C. Liu, T.-Y. Yan, C.-Y. Yue and X.-W. Lei, Water-Stable 0d Hybrid Manganese Halides with Adjustable Crystal Structure and Emission Color, *Adv. Opt. Mater.*, 2023, **11**, 2301010.
14 G. Xu, C. Wang, Y. Li, W. Meng, G. Luo, M. Peng, B. Xu and Z. Deng, Solid-State Synthesis of Cesium Manganese

Halide Nanocrystals in Glass with Bright and Broad Red Emission for White LEDs, *Chem. Sci.*, 2023, **14**, 5309–5315.
15 D. Jin, Y. Lu, R. C. Leif, S. Yang, M. Rajendran and L. W. Miller, How to Build a Time–Gated Luminescence Microscope, *Curr. Protoc. Cytom.*, 2014, **67**, 2.22.1–2.22.36.
16 B. Su, G. Zhou, J. Huang, E. Song, A. Nag and Z. Xia, Mn^{2+}-Doped Metal Halide Perovskites: Structure, Photoluminescence, and Application, *Laser Photonics Rev.*, 2021, **15**, 2000334.
17 S. Xiong, Y. Xiong, D. Wang, Y. Pan, K. Chen, Z. Zhao, D. Wang and B. Z. Tang, Achieving Tunable Organic Afterglow and UV-Irradiation-Responsive Ultralong Room-Temperature Phosphorescence from Pyridine-Substituted Triphenylamine Derivatives, *Adv. Mater.*, 2023, **35**, 2301874.
18 X. Wang, Z. Qiu, Y. Liang, Z. Song, S. Li, J. Zhang and S. Lian, Achieving Dynamic Multicolor Luminescence in ZnS:KBr,Mn^{2+} Phosphor for Anti-Counterfeiting, *Chem. Eng. J.*, 2022, **429**, 132537.
19 X. Zhou, K. Han, Y. Wang, J. Jin, S. Jiang, Q. Zhang and Z. Xia, Energy-Trapping Management in X-Ray Storage Phosphors for Flexible 3D Imaging, *Adv. Mater.*, 2023, **35**, 2212022.
20 K. Huang, X. Dou, Y. Zhang, X. Gao, J. Lin, J. Qu, Y. Li, P. Huang and G. Han, Enhancing Light and X-Ray Charging in Persistent Luminescence Nanocrystals for Orthogonal Afterglow Anti-Counterfeiting, *Adv. Funct. Mater.*, 2021, **31**, 2009920.
21 X. Chen, X. Wang, X. Zhang and Y. Zhang, Mn^{2+}-Activated Afterglow in a Transparent Perovskite Crystal, *J. Phys. Chem. Lett.*, 2022, **13**, 8163–8168.
22 W. Zheng, X. Li, N. Liu, S. Yan, X. Wang, X. Zhang, Y. Liu, Y. Liang, Y. Zhang and H. Liu, Solution-Grown Chloride Perovskite Crystal of Red Afterglow, *Angew. Chem., Int. Ed.*, 2021, **60**, 24450–24455.
23 Y. Liu, X. Zhang, X. Wang, S. Yan, Y. Liang and Y. Zhang, Ultralong Afterglow and Unity Quantum Yield from a Transparent $CsCdCl_3$:Mn Crystal, *Aggregate*, 2023, **4**, e334.
24 F. Jiang, Z. Wu, M. Lu, Y. Gao, X. Li, X. Bai, Y. Ji and Y. Zhang, Broadband Emission Origin in Metal Halide Perovskites: Are Self-Trapped Excitons or Ions?, *Adv. Mater.*, 2023, **35**, 2211088.
25 H. Arfin, A. S. Kshirsagar, J. Kaur, B. Mondal, Z. Xia, S. Chakraborty and A. Nag, ns^2 Electron (Bi^3+ and Sb^{3+}) Doping in Lead-Free Metal Halide Perovskite Derivatives, *Chem. Mater.*, 2020, **32**, 10255–10267.
26 Y. Shi, X. Zhang, X. Chen and Y. Zhang, Trap-Tuning in Afterglow Perovskite Crystals through Alkali Metal Ion Doping, *Chem. Commun.*, 2022, **58**, 10048–10051.
27 L. Cao, X. Jia, W. Gan, C.-G. Ma, J. Zhang, B. Lou and J. Wang, Strong Self-Trapped Exciton Emission and Highly Efficient near-Infrared Luminescence in Sb^{3+}-Yb^{3+} Co-Doped $Cs_2AgInCl_6$ Double Perovskite, *Adv. Funct. Mater.*, 2023, **33**, 2212135.
28 Y. Zhang, X. Liu, H. Sun, J. Zhang, X. Gao, C. Yang, Q. Li, H. Jiang, J. Wang and D. Xu, Strong Self-Trapped Exciton Emissions in Two-Dimensional Na-In Halide Perovskites Triggered by Antimony Doping, *Angew. Chem., Int. Ed.*, 2021, **60**, 7587–7592.
29 B. Ke, R. Zeng, Z. Zhao, Q. Wei, X. Xue, K. Bai, C. Cai, W. Zhou, Z. Xia and B. Zou, Homo- and Heterovalent Doping-Mediated Self-Trapped Exciton Emission and Energy Transfer in Mn-Doped $Cs_2Na_{1-x}Ag_xBiCl_6$ Double Perovskites, *J. Phys. Chem. Lett.*, 2020, **11**, 340–348.
30 W. Stadler, D. M. Hofmann, H. C. Alt, T. Muschik, B. K. Meyer, E. Weigel, G. Müller-Vogt, M. Salk, E. Rupp and K. W. Benz, Optical Investigations of Defects $InCd_{1-x}Zn_xTe$, *Phys. Rev. B: Condens. Matter Mater. Phys.*, 1995, **51**, 10619–10630.
31 W. Zhang, P. Sui, W. Zheng, L. Li, S. Wang, P. Huang, W. Zhang, Q. Zhang, Y. Yu and X. Chen, Pseudo–2d Layered Organic–Inorganic Manganese Bromide with a near–Unity Photoluminescence Quantum Yield for White Light–Emitting Diode and X–Ray Scintillator, *Angew. Chem., Int. Ed.*, 2023, **62**, e202309230.
32 Y. Wang, T. Zhou, J. Chen, H. Qin, J. Wu, Q. Zhang, J. Zheng, X. Li, Y. Y. Sun, Y. He, X. Ma, T. Ye, R. Liu, Z. Gao, J. Hou, L. Wang, H. Chen and W. Jiang, Zero–Dimensional Organic–Inorganic Hybrid Zinc Halides for Multiple Applications in Anti–Counterfeiting, X–Ray Imaging and White LEDs, *Adv. Opt. Mater.*, 2023, 2301864.
33 J. A. Steele, P. Puech, M. Keshavarz, R. Yang, S. Banerjee, E. Debroye, C. W. Kim, H. Yuan, N. H. Heo, J. Vanacken, A. Walsh, J. Hofkens and M. B. J. Roeffaers, Giant Electron–Phonon Coupling and Deep Conduction Band Resonance in Metal Halide Double Perovskite, *ACS Nano*, 2018, **12**, 8081–8090.
34 A. C. Dakshinamurthy and C. Sudakar, Influence of the Octahedral Cation on the Evolution of Lattice Phonons in Metal Halide Double Perovskites: Raman Spectroscopic Investigation of $Cs_2B'B''Cl_6$ ($B'=Ag_{1-x}Na_x$; $B''=Bi_{1-x}In_x$), *Phys. Rev. Mater.*, 2023, **7**, 065401.
35 Z. Wang, Y. Chen, J. Ke, Y. Wei, Y. Liu and M. Hong, Achieving Ultra-Broadband near-Infrared Emission in Cr^{3+}-Activated $Cs_2NaScCl_6$ Perovskite for Efficient Phosphor-Converted Light-Emitting Diodes, *Adv. Opt. Mater.*, 2023, 2301323.
36 H. Yang, X. Chen, H. Lu, Y. Li, W. Sun, Y. Zhang, X. Liu, G. Long, L. Zhang and X. Li, Self-Trapped Excitons-Based Warm-White Afterglow by Room-Temperature Engineering toward Intelligent Multi-Channel Information System, *Adv. Funct. Mater.*, 2023, 2311437.
37 Z. Wang, Z. Song, L. Ning and Q. Liu, Sunlight-Activated Yellow Long Persistent Luminescence from Nb-Doped Sr_3SiO_5:Eu^{2+} for Warm-Color Mark Applications, *J. Mater. Chem. C*, 2020, **8**, 1143–1150.